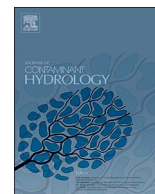




Contents lists available at ScienceDirect

Journal of Contaminant Hydrology

journal homepage: [www.elsevier.com/locate/jconhyd](http://www.elsevier.com/locate/jconhyd)

## Modelling and upscaling of transport in carbonates during dissolution: Validation and calibration with NMR experiments

Bagus P. Muljadi<sup>a,\*</sup>, Branko Bijeljic<sup>a</sup>, Martin J. Blunt<sup>a</sup>, Adam Colbourne<sup>b</sup>, Andy J. Sederman<sup>b</sup>, Mick D. Mantle<sup>b</sup>, Lynn F. Gladden<sup>b</sup>

<sup>a</sup> Department of Earth Science and Engineering, Imperial College, Prince Consort Road, London SW7 2BP, United Kingdom

<sup>b</sup> Department of Chemical Engineering, University of Cambridge, Pembroke Street, Cambridge CB2 3RA, United Kingdom

### A B S T R A C T

We present an experimental and numerical study of transport in carbonates during dissolution and its upscaling from the pore ( $\sim \mu\text{m}$ ) to core ( $\sim \text{cm}$ ) scale. For the experimental part, we use nuclear magnetic resonance (NMR) to probe molecular displacements (propagators) of an aqueous hydrochloric acid (HCl) solution through a Ketton limestone core. A series of propagator profiles are obtained at a large number of spatial points along the core at multiple time-steps during dissolution. For the numerical part, first, the transport model—a particle-tracking method based on Continuous Time Random Walks (CTRW) by Rhodes et al. (2008)—is validated at the pore scale by matching to the NMR-measured propagators in a beadpack, Bentheimer sandstone, and Portland carbonate (Scheven et al., 2005). It was found that the emerging distribution of particle transit times in these samples can be approximated satisfactorily using the power law function  $\psi(t) \sim t^{-1-\beta}$ , where  $0 < \beta < 2$ . Next, the evolution of the propagators during reaction is modelled: at the pore scale, the experimental data is used to calibrate the CTRW parameters; then the shape of the propagators is predicted at later observation times. Finally, a numerical upscaling technique is employed to obtain CTRW parameters for the core. From the NMR-measured propagators, an increasing frequency of displacements in stagnant regions was apparent as the reaction progressed. The present model predicts that non-Fickian behaviour exhibited at the pore scale persists on the centimetre scale.

### 1. Introduction

Transport and reaction of fluids in porous media is important in many hydrogeological problems. Examples include stimulation in petroleum reservoirs by acidization (Fredd et al., 2017), water and contaminant management (Singurindy et al., 2004), and geological storage of carbon dioxide (Herzog et al., 2003; Luquot and Gouze, 2009). Rock matrix dissolution refers to reactions at fluid/solid boundaries that result in the dissolution of the solid grains, pore growth, and variation of flow characteristics. For practical applications, the main difficulties in building models with predictive capabilities are twofold: first, reaction changes the microstructure of the rock, and thus the structure heterogeneity starting at the pore scale. Second, there is a large disparity between the scale at which transport can be understood from first principles, and the scale at which practical predictions are needed (Scheibe et al., 2015). Since in many cases, the formal closure problem may be too complex for general solution, we propose to study the

effects of reaction on solute transport from micrometre to centimetre scales using a heuristic multiscale modelling approach which does not impose a particular form to the governing equations, in conjunction with NMR fluid propagator method to validate and calibrate the model at the pore scale sequentially during dissolution.

The heterogeneity of porous media in geological formations is embodied by the pore structure as well as the mineralogical heterogeneity resulting from multiple components. In heterogeneous porous media, the observed reactive transport processes frequently do not behave according to the transport laws that can be derived for homogeneous media, see Kang et al. (2014), Liu et al. (2015), Molins et al. (2012), Ovaysi and Piri (2014), Szymczak and Ladd (2009) and Tartakovsky et al. (2007), such as the classical advection-diffusion-reaction equations. Because reactive transport modelling is typically applied at large scales, it necessarily ignores spatial heterogeneities at scales smaller than the size of model discretization, see Li et al. (2006) and Noirel et al. (2004). Several techniques have been introduced as a remedy, i.e.

\* Corresponding author at: Department of Chemical and Environmental Engineering, University of Nottingham, University Park, Nottingham NG7 2RD, United Kingdom.

E-mail addresses: [Bagus.Muljadi@nottingham.ac.uk](mailto:Bagus.Muljadi@nottingham.ac.uk) (B.P. Muljadi), [b.bijeljic@imperial.ac.uk](mailto:b.bijeljic@imperial.ac.uk) (B. Bijeljic), [m.blunt@imperial.ac.uk](mailto:m.blunt@imperial.ac.uk) (M.J. Blunt), [ac937@cam.ac.uk](mailto:ac937@cam.ac.uk) (A. Colbourne), [ajs40@cam.ac.uk](mailto:ajs40@cam.ac.uk) (A.J. Sederman), [mdm20@cam.ac.uk](mailto:mdm20@cam.ac.uk) (M.D. Mantle), [lfg1@cam.ac.uk](mailto:lfg1@cam.ac.uk) (L.F. Gladden).

<http://dx.doi.org/10.1016/j.jconhyd.2017.08.008>

Received 31 March 2017; Received in revised form 20 August 2017; Accepted 23 August 2017

0169-7722/© 2017 The Authors. Published by Elsevier B.V. This is an open access article under the CC BY license (<http://creativecommons.org/licenses/by/4.0/>).

**Nomenclature****Acronyms**

CTRW	continuous time random walk
PFG	pulsed field gradient
PTM	particle-tracking method
TPL	truncated-power law

**Greek symbols**

$\langle \zeta \rangle_0$	mean particle displacement m
$\beta$	power-law coefficient
$\Delta$	NMR observation time s
$\phi$	porosity
$\psi(t)$	transit-time distribution
$\tau$	normalized time $t/t_1$
$\zeta$	particle displacement m

**Roman symbols**

$A$	normalization constant
$d$	core diameter m

$D_m$	diffusion coefficient $\text{m}^2 \text{s}^{-1}$
$Da$	Damköhler number
$l$	core length m
$P$	probability density function
$p(i, j)$	probability of a particle moving from $i$ to $j$
$Pe$	Péclet number
$Q$	flux of fluid $\text{m}^3 \text{s}^{-1}$
$t$	transit time s
$t_1$	average advection time s
$t_2$	diffusion cut-off time s
$t_{\text{exp}}$	experimental time s
$v$	interstitial velocity $\text{m s}^{-1}$

**Subscripts**

$C$	core scale
$CP$	core-plug scale
$i, j$	node indices
$k$	link indices
$P$	pore scale

to compute effective parameters which capture subscale effects, see [Chastanet and Wood \(2008\)](#) and [Porta et al. \(2013\)](#). Furthermore, while under limited circumstances the homogeneity assumption is reasonable, the pore-scale heterogeneities can result in a significant “scaling effect” because of the spatial variations of concentrations and reaction rates, leading to the breakdown of the homogeneity assumption. This scaling effect may be one of the causes of the order-of-magnitude differences between laboratory measured reaction rates and that obtained from field measurements, see [Li et al. \(2006\)](#) and [Steeffel et al. \(2005\)](#). Therefore, it is important to understand the effects of pore-scale heterogeneities on the reactive transport processes.

Conventionally transport simulation is performed by solving the advection-dispersion equation (ADE) with known, albeit complicated, boundary condition. In some cases, depending on the investigated conditions and on the quality of the characterisation of the heterogeneity of the system, the ADE can still be used effectively, see [Riva et al. \(2008\)](#). Furthermore, it is difficult to determine the correct values of the coefficients in the model. As the solution of the ADE at a fine scale over the full extent of the geological heterogeneity is prohibitively difficult, as we have no general way to incorporate uncertainty in the description of the reservoir model for the prediction of transport. Motivated by this problem, [Rhodes et al. \(2008, 2009\)](#) presented a particle-tracking method based on CTRW (from here-on called PTM-CTRW) for solving single-phase transport across a hierarchy of length-scales. Unlike other upscaling methods which rely on special basis functions, or homogenisation to capture the subscale effects (see [Degond et al., 2015](#); [Muljadi, 2017](#); [Muljadi et al., 2015](#); [Porta et al., 2013](#)), the method does not pre-suppose the functional form of the upscaled transport equations, and automatically accounts for uncertainty in the field-scale description. PTM-CTRW has been tested for simulating transport in sandstones. Here, PTM-CTRW forms the basis of our solute transport

simulations and its application is extended to reactive transport in carbonates.

To rid geological transport simulation of uncertainties due to up-scaling, it is imperative that a numerical model undergoes rigorous laboratory validations. In our study, the model and its validation are built upon pore-scale information. The distribution of molecular displacement (or propagators) in the preasymptotic dispersion regime can provide the basis for validation of transport models that are based on X-ray microtomography images of the pore space — see [Bijeljic et al. \(2013a,b\)](#) and [Yang et al. \(2013\)](#). In recent years, Nuclear Magnetic Resonance (NMR) has been used to probe transport signatures in porous glass beads, see [Scheven et al. \(2004\)](#). It has also been used in beadpack, sandstone and carbonate samples in the preasymptotic dispersion regimes e.g. in [Scheven et al. \(2005\)](#) and [Mitchell et al. \(2008\)](#). This paper augments previous work and describes how NMR 1D-imaging and fluid propagator measurements are employed to provide experimental insights of hydrochloric acid (HCl) flow through Ketton carbonate cores at multiple time increments during dissolution. First, HCl solution is injected into the core as illustrated in [Fig. 1](#). The change in porosity, and propagators at a large number of spatial points along the core can be monitored throughout the experiment. These propagators are then used to calibrate our model at a pore ( $\sim \mu\text{m}$ ), and core-plug scale ( $\sim \text{mm}$ ), as well as to derive the local probability density functions (PDFs) of transit times, the combination of which, will be used to derive the PDF at the core scale ( $\sim \text{cm}$ ).

The scope of this work can be summarized as follows. First, PTM-CTRW is employed to reproduce the NMR-measured propagators through a beadpack, Bentheimer sandstone, and Portland carbonate cores and thereby validate the described model. Second, the pulsed field gradient NMR technique is used to find a series of reactive propagators in preasymptotic flow through Ketton carbonate core at

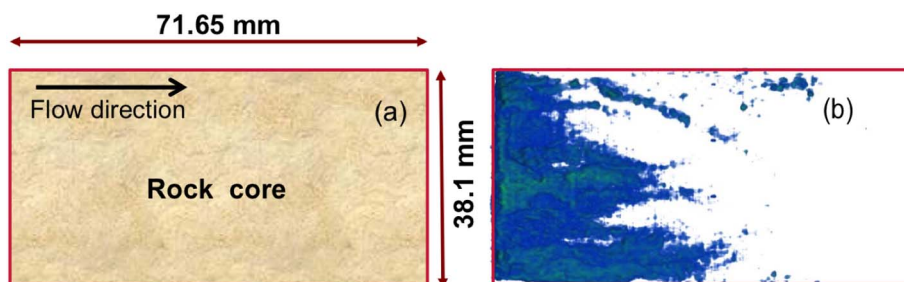


**Fig. 1.** A reactive transport experiment where HCl solution is injected through a core of Ketton limestone core. Flow channels are formed due to solid dissolution. The figures depict (a) the dimension of the core, and (b) the difference in porosity between the beginning and the end of the experiment provided using NMR imaging, with blue being the smallest and green the largest; white indicates no change in porosity. (For interpretation of the references to color in this figure legend, the reader is referred to the web version of this article.)

multiple times during dissolution. Third, these propagators are reproduced numerically, an array of time-transit distributions is obtained, and thereby calibrate the present model at the pore scale. Finally, these propagators are used as the bases of our core-scale simulation and derive the upscaled CTRW parameters at the beginning and the end of the experiments. This model can then be used to predict transport at any scale of interest.

## 2. Continuous time random walks

The description of CTRW here is by no means exhaustive; for details on the application of CTRW in a geological context, the reader is referred to an excellent review by Berkowitz et al. (2006).

Anomalous or non-Fickian transport is prevalent in heterogeneous porous media, and is ubiquitous in the context of tracer migration in geological formations. Anomalous transport can be described elegantly as a continuous time random walk. In a CTRW framework, dispersion, which results in solute spreading at the scale of observation, is accounted for by a transit time distribution function  $\psi(t)$ . For many systems,  $\psi(t)$  exhibits power-law dependencies:  $\psi(t) \sim t^{-1-\beta}$ , where  $\beta \leq 2$  is an exponent. For such systems, this leads to the scaling of outlet concentration  $C(t) \sim t^{-1-\beta}$ , see Nunes et al. (2015).

## 3. Transport model description

Traditionally CTRW has been applied to find the ensemble average behaviour of a plume in a macroscopically homogenous domain, see Berkowitz et al. (2006) and Dentz et al. (2004). CTRW has been applied to heterogeneous media, but for relatively coarsely gridded two-dimensional systems where the solution involves the numerical inversion of a multi-dimensional Laplace transform, see Cortis et al. (2004). Rhodes et al. (2008, 2009) developed a simpler approach, PTM-CTRW, to describe transport spanning across microns to kilometre scales. The stochastic framework also allows more complicated boundary

conditions and various types of distribution function to be used. Here the modelling framework according to PTM-CTRW is explained, in which transport is seen as a series of random hops from one node in a 3D lattice to its neighbouring node. Particles move between a series of discrete nodes or sites with a probability  $\psi(t : i, j)$  that a particle that first arrives at site  $i$  will move to site  $j$  in a time  $t + dt$ .

At the heart of PTM-CTRW is the *correct* choice of transit-time distribution  $\psi(t)$ . In their pore-scale simulation, Rhodes et al. (2008) employed two types of transit-time distribution, one derived from the advection-diffusion equation, as presented in Bijeljic et al. (2004), and another a truncated power-law function as an ensemble averaged transit-time distribution, presented in Dentz et al. (2004). They conducted numerical studies comparing the two functions; the former was employed in a 3D lattice with a Berea sandstone derived distribution of throat radii, while the latter was implemented in an effective homogenous lattice. They compared the results from both methods with experimental data for Berea sandstone and found that the truncated power-law function gave the observed transport behaviour and reproduced the dispersion coefficients obtained from experiments accurately. The truncated power-law (TPL) transit-time distribution function, as presented in Dentz et al. (2004), is

$$\psi(t) = Ae^{-t/t_2}(1+t/t_1)^{-1-\beta}, \quad (1)$$

where  $A$  is a normalization constant such that  $\int_0^t \psi(t') dt' = 1$ , and  $\beta \leq 2$  is a power-law coefficient.

Using network modelling of transport, Bijeljic and Blunt (2006) were able to match the transit-time probability density function measured in links between neighbouring pores of a Berea sandstone pore network using Eq. (1) with  $\beta = 1.8$ . Furthermore, Bijeljic et al. (2011) performed direct simulations of transport in the pore spaces of micro-CT images of Berea sandstone and Portland carbonate and obtained  $\beta = 1.8$  and  $\beta = 0.7$  respectively. Transit times were now measured as the time particles to migrate from one pore voxel to another.

At the Darcy scale, an explicit relationship between the histogram of

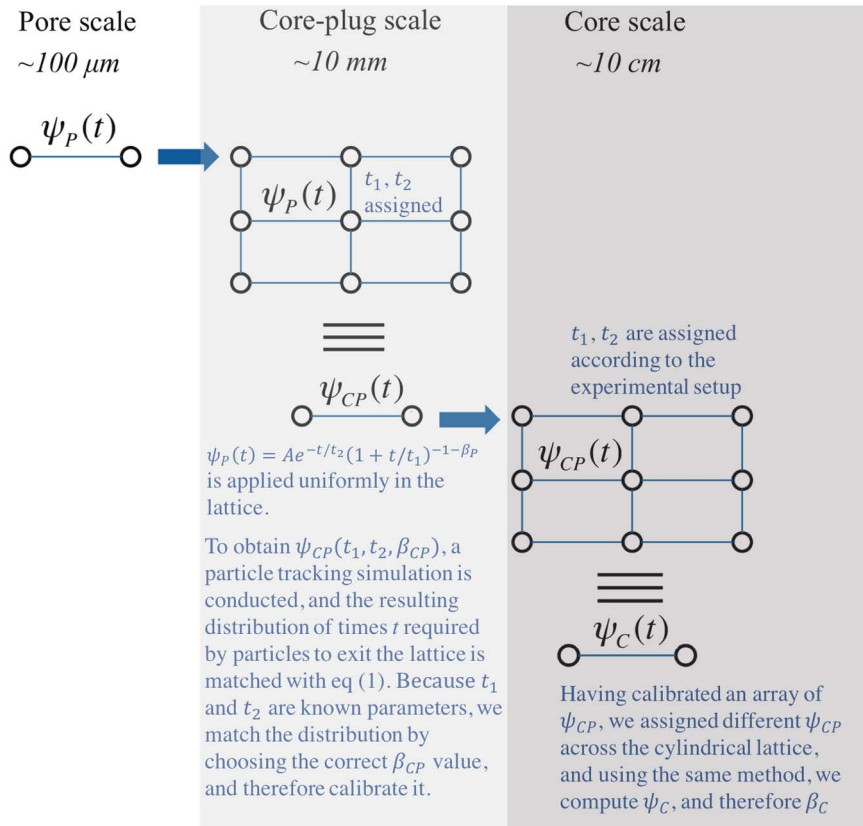


**Fig. 2.** The pore-to-core simulation technique. Transport is modelled as a series of hops between nodes via links with a known transit time distribution  $\psi(t)$ . At the smallest scales, advective and diffusive transport is simulated through a lattice representing the porous medium of interest. Transport from one pore to another is described by  $\psi_P$  that is averaged over all possible statistical realizations of the structure. This  $\psi_P(t)$  is then input into a simulation at the core-plug scale to compute  $\psi_{CP}(t)$  for transitions of particles over the mm scale. Finally, transport at a core scale can be represented as a single hop governed by the transit-time distribution function  $\psi_C(t)$ .

Source: This figure is adapted from Rhodes et al. (2008)

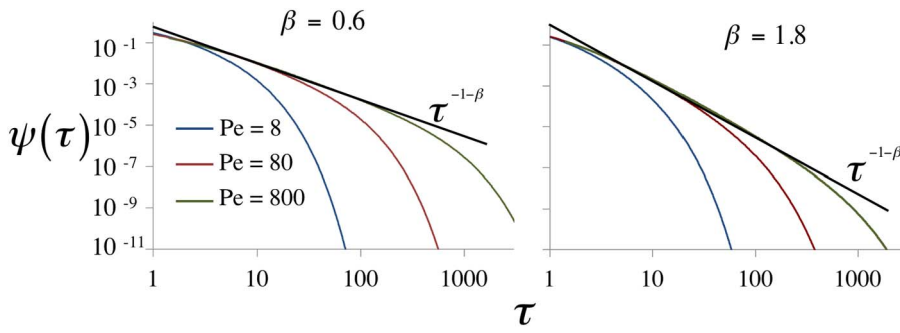


Fig. 3.  $\psi$  as a function of  $\tau = t/t_1$ . (left)  $\beta = 0.6$ , and (right)  $\beta = 1.8$ , for several  $Pe$  numbers using Eq. (1).

permeability and  $\beta$  has been demonstrated (Edery et al., 2014). Here, a truncated power-law is also used to describe small-scale transport, where the exponent  $\beta$  exponent acts as a measure of heterogeneity. In Fig. 2, the pore-to-core transport simulation framework is described.

To clarify the implementation of our method, in Fig. 3 we show the behaviour of  $\psi$  given the variety of its parameters. We plot Eq. (1) where  $\psi$ , is a function of the normalized time  $\tau = t/t_1$  for several Péclet numbers  $Pe = 2t_2/t_1$ . The left figure shows  $\psi$  for  $\beta = 0.6$ , and the right figure  $\beta = 1.8$ . At larger  $\beta$ , the long-time distribution diminish faster as illustrated by the power-law trend  $\psi \sim \tau^{-1-\beta}$ .

At the pore scale ( $\sim \mu\text{m}$ ), a transit time distribution function  $\psi_p(t)$  is derived from either a semi-analytic description in an idealized network, or from direct simulation.  $\psi_p(t)$  will form the basis of simulation at the core-plug scale ( $\sim \text{mm}$ ). Numerical upscaling will be implemented such that transport at this scale can be modelled as a single hop governed by a transit-time distribution  $\psi_{CP}(t)$ . For the core-scale simulation ( $\sim \text{cm}$ ), a lattice is used that is similar in shape to the rock core used in the experiments—a cylinder—in which  $\psi_{CP}(t)$  is applied in each link, this core-scale lattice will be calibrated a priori. Numerical upscaling will then be used again to obtain  $\psi_C(t)$  (see Section 6).

In the pore-scale simulation, transport is simulated on a homogeneous 3D lattice consisted of nodes and links. Within each link, transport is governed by the transit-time distribution function  $\psi_p(t)$ , Eq. (1). First, a pressure difference is assigned at the inlet and outlet faces. Then the pressure field is solved by enforcing mass balance at each node, assuming slow, single-phase, Newtonian flow. At each node, the mass-flux ( $q$ ) conservation  $\sum_k q_k = 0$  is applied for each node connected to links  $k$  by which the velocity field at each link can be known, see Appendix A for details. Assuming complete mixing at each node, the probability  $p(i,j)$  that a particle landing at pore  $i$  will move to one of its neighbours is calculated

$$p(i, j) = \frac{Gq_{ij}}{1 - e^{-Pe_{ij}}}; \quad \text{if } q_{ij} > 0$$

$$p(i, j) = \frac{Gq_{ji}}{e^{Pe_{ij}} - 1}; \quad \text{if } q_{ij} < 0$$
(2)

where  $q_{ij}$  is the flux in a link connecting node  $i$  and  $j$ , and  $G$  is a normalization coefficient such that  $\sum_j p(i, j) = 1$ , i.e.,

$$\frac{1}{G} = \sum_{q_{ij} > 0} \frac{q_{ij}}{1 - e^{-Pe_{ij}}} + \sum_{q_{ij} < 0} \frac{q_{ji}}{e^{Pe_{ij}} - 1}.$$
(3)

Then a number of particles are released either at the inlet face, or randomly in the lattice.

At an intersection, a random number  $a$  is generated.  $P(i,j)$  is then read from memory, and defined as  $P(i, j) = \sum_m p(i, m)$ ;  $m \leq j$ . The process is iterated such that

$$P(i, j - 1) \leq a \leq P(i, j).$$
(4)

When Eq. (4) is satisfied, the particle will move along the link  $i-j$ . A random number  $z$  is generated and the time  $t$  required to move along the link  $i-j$  is found by solving, using a root-finding method,  $F(t) = z$  i.e.,

$$F(t) = \int_0^t \psi_p(t) dt = z$$
(5)

where

$$\psi_p(t) = Ae^{-t/t_2}(1+t/t_1)^{-1-\beta}$$
(6)

and  $t_1 = l/v$ ,  $l$  is the link length and  $v$  is the fluid velocity within that link.  $t_2 = l^2/D_m$  is the cut-off diffusion time, and  $D_m$  is the self-diffusion coefficient of the working fluid.  $v$  and  $D_m$ , thus  $t_1$  and  $t_2$  are known a priori; leaving the adjustable parameter  $\beta$  that describes transport heterogeneity.

To obtain the transit-time distribution at the next larger scale, the same technique as in Rhodes et al. (2008) is used, i.e. a number of particles at  $t = 0$  is released at the inlet face of a 3D lattice and the time required for each particle to transit recorded.  $\psi(t)$  can be obtained at the next larger scale by matching the emergent distribution of the transit times of each particle to Eq. (1). This is illustrated in Fig. 4 where  $\psi_s(t)$  is the transit time distribution function at a scale larger than where transport is governed by  $\psi_p(t)$ . This methodology is applied to obtain both  $\psi_{CP}(t)$  from  $\psi_p(t)$ , and  $\psi_C(t)$  from  $\psi_{CP}(t)$ .

#### 4. Experimental technique, apparatus and results

In this paper, pulsed field gradient nuclear magnetic resonance (PFG-NMR) is used to obtain propagator measurements, i.e. probability distributions,  $P(\zeta)$ , of molecular displacement for a given observation time ( $\Delta$ ) as described in Kärger and Heink (1983). Here, the experiments are applied such that the water, resident in the rock core, is studied. By observing the displacement,  $\zeta$ , of water molecules over a range of observation times  $\Delta$  and flow velocities  $v$ , the fluid behaviour and pore-scale heterogeneity can be characterised. These experiments are time-consuming when the data is fully sampled, requiring experimental durations of the order of hours to complete which is impractical

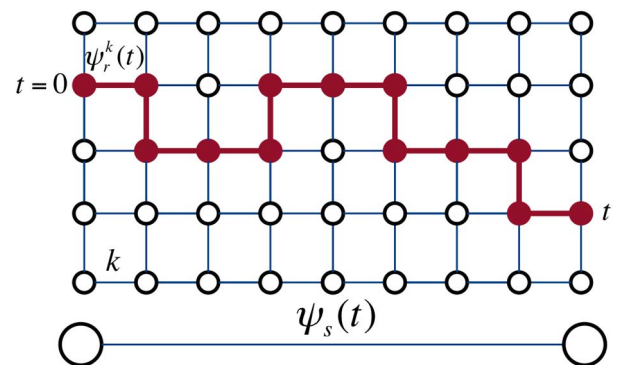


Fig. 4. The upscaling methodology. First, flow in each link is solved such that  $t_1$  and  $t_2$  can be determined. Then a number of particles are launched at the inlet face at  $t = 0$ . The time required for one particle to reach the outlet face is that particle's transit time.  $\psi_p^k(t)$  is the transit-time distribution function governing transport in link  $k$ .  $\psi_s(t)$  is obtained by matching the emergent transit-time distribution with Eq. (1).

for the study of the dynamic, reacting system being investigated here. In this work, we have reduced the data acquisition time through undersampling and reconstruction of the smooth acquisition domain signal. Further details of the sampling and reconstruction parameters used here can be found are described in Colbourne et al. (2016).

For the reaction, 10 l of a 0.01 M HCl solution was flowed at  $Q = 8.3 \times 10^{-7} \text{ m}^3 \text{ s}^{-1}$ , through a 7.2 cm long by 3.81 cm diameter sample of Ketton limestone. Propagators are recorded in 0.88 cm slices along the core with an observation time ( $\Delta$ ) of 0.25 s. In each slice, the porosity  $\phi$  and propagator are measured throughout the dissolution process with porosity profile measurements being acquired in 0.5 min and the propagator measurements being acquired in 14.5 min using the undersampling methods described in Colbourne et al. (2016).

The diffusion coefficient  $D_m$  of water, in water, at 293 K is  $2.1 \times 10^{-9} \text{ m}^2 \text{ s}^{-1}$ . The initial porosity of the core  $\phi$  is 0.24. The interstitial velocity  $v$  is  $\frac{(Q/A)}{\phi} = 3.06 \times 10^{-3} \text{ m s}^{-1}$ . The characteristic length  $l$  of the Ketton limestone can be estimated i.e.,  $l = \pi/S$ , where  $S [\text{m}^{-1}]$  is the specific surface area, such that  $l = 4.07 \times 10^{-4} \text{ m}$ , as presented in Mostaghimi et al. (2013). The corresponding Péclet number,  $Pe = lv/D_m$ , is therefore 593. The Damköhler number, the ratio of acid consumed and the acid transported by convection, is defined in Menke et al. (2016) as,

$$Da = \frac{\pi r}{vn} \quad (7)$$

where  $r$  is the reaction rate constant of pure calcite in 0.01 M HCl solution at 293 K ( $1.5 \times 10^{-3} \text{ mol m}^{-2} \text{ s}^{-1}$ ) measured experimentally in Peng et al. (2015).  $n$  is calculated using  $n = \rho_{\text{calcite}}[1 - \phi]/M_{\text{calcite}} \cdot \rho_{\text{calcite}}$  is the density of pure calcite ( $2.71 \times 10^3 \text{ kg m}^{-3}$ ), and  $M_{\text{calcite}}$  is the molecular mass of calcite ( $0.1 \text{ kg mol}^{-1}$ ). In our experiment,  $Da = 7.7 \times 10^{-5}$ .

Fig. 5 shows the propagators as a function of axial position along the core-plug, before and after dissolution. Before reaction, the propagators are uniform along the length of the core, showing a sharp stagnant region centred on 0 displacement and a broad flowing region extending to a displacement of  $\sim 3.5 \text{ mm}$ . After dissolution of the solid matrix has taken place, predominantly in the first half of the core, the propagators in this region evolve — fast moving fluid slows as the pore-space is opened up and the overall porosity is increased.

## 5. Model validation

### 5.1. Comparison with NMR-measured propagators in a beadpack, Bentheimer sandstone, and Portland carbonate

The results of the numerical methods are now compared with the NMR-measured propagators, without reaction, transport only (Scheven

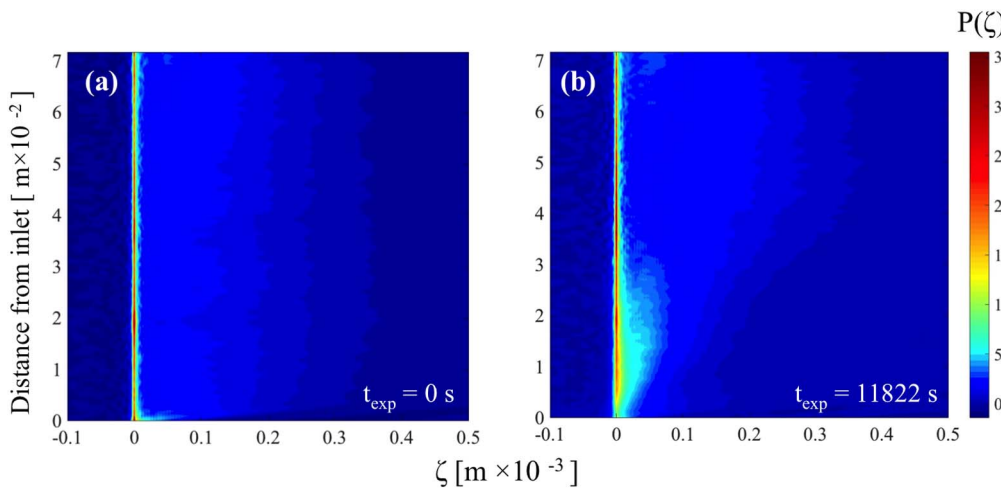


Fig. 5. Experimental results showing the NMR propagator contour at (a)  $t_{\text{exp}} = 0 \text{ s}$ —the beginning of the experiment; and at (b)  $t_{\text{exp}} = 11,800 \text{ s}$ —the end of the experiment. The average flow velocity  $v$  is  $3.06 \times 10^{-3} \text{ m s}^{-1}$ , and the observation time  $\Delta$  is 0.25 s. The propagator  $P(\zeta)$  consists of the normalized probability of displacement  $\zeta$  such that  $\int_{\zeta} P(\zeta) d\zeta = 1$ .

et al., 2005) in a beadpack, Bentheimer sandstone, and Portland carbonate.

The computational domain is a homogenous  $0.008 \times 0.008 \times 0.008 \text{ m}^3$  lattice consisting of  $80 \times 80 \times 80$  links. In this analysis, the system is homogeneous at the core scale and the measurements of displacement are taken across the whole core. In these computations, the same interstitial velocities are used as in the experiments, namely  $v = 9.1 \times 10^{-4}$ ,  $1.03 \times 10^{-3}$ , and  $1.26 \times 10^{-3} \text{ m s}^{-1}$  for beadpack, Bentheimer sandstone, and Portland carbonate respectively. Particles are launched at random locations in the lattice at  $t = 0 \text{ s}$  and their movement is tracked. If a particle exits the inlet or outlet, it is randomly reassigned to the opposite face using a flux-weighted assignment.

The propagators were measured at different  $\Delta$ . The propagators were computed using the transit-time distribution, Eq. (1). Average advection times  $t_1 = 0.11, 0.097$ , and  $0.079 \text{ s}$  are known from the interstitial velocities  $v$  and the cut-off diffusion time is  $t_2 = l^2/D_m = 15 \text{ s}$ . By fitting the power-law exponent  $\beta$ s, it was possible to match the experimental data:  $\beta = 1.96, 1.76$ , and  $0.63$  yield propagator profiles with those of a beadpack, Bentheimer sandstone, and Portland carbonate respectively, at all studied observation times, as shown in Fig. 6. The experiments therefore calibrate our model at the pore scale. As expected, transport is the most heterogeneous in the Portland sample, and the least in the beadpack. Our model matches the persistently dominant stagnant region in the Portland sample, which is a manifestation of transport heterogeneity. This is discussed in more detail in Bijeljic et al. (2013b).

### 5.2. Comparison with NMR experiments of transport involving mineral dissolution

The propagators obtained from NMR measurement of reactive transport experiments are now reproduced. The model is calibrated with experimental data of porosities  $\phi$  and propagators in a number of slices along the sample measured at the beginning and the end of the dissolution process. Transport in each slice of the core is computed in a lattice consisting of  $100 \times 100 \times 100$  links representing a cube of side length  $8 \times 10^{-3} \text{ m}$ . Each link in the lattice has a length of  $8 \times 10^{-5} \text{ m}$ , which is the resolution of our pore-scale simulation. 100,000 particles are launched at random locations in the lattice at  $t = 0 \text{ s}$ . Periodic boundary conditions are applied at the inlet and outlet faces. If a particle exits the inlet or outlet, it is randomly reassigned to the opposite face using a flux-weighted rule. At this scale, transport is governed by  $\psi_P$  according to Eq. (1). The CTRW parameters  $t_1, t_2$  are computed using the knowledge of flow rate  $Q = 8.3 \times 10^{-7} \text{ m}^3 \text{ s}^{-1}$ , molecular diffusion coefficient, and porosity  $\phi$  within that slice, from which interstitial velocity  $v$  can be computed. For example, for the slice with initial porosity  $\phi = 0.24$ , the initial interstitial velocity is

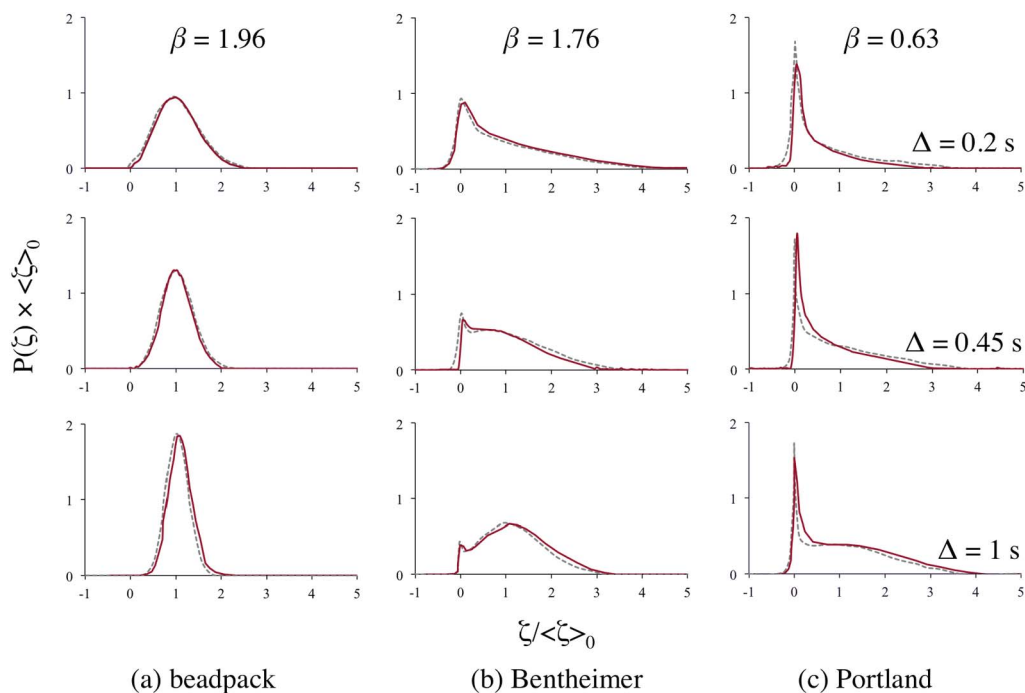


Fig. 6. Computed probability of particle displacement  $P(\xi) \times \langle \xi \rangle_0^{-1}$  as a function of displacement  $\xi / \langle \xi \rangle_0$  (solid lines), compared with the propagators obtained with NMR experiments by Scheven et al. (2005) (dashed lines) for  $\Delta = 0.2, 0.45$ , and  $1$  s.

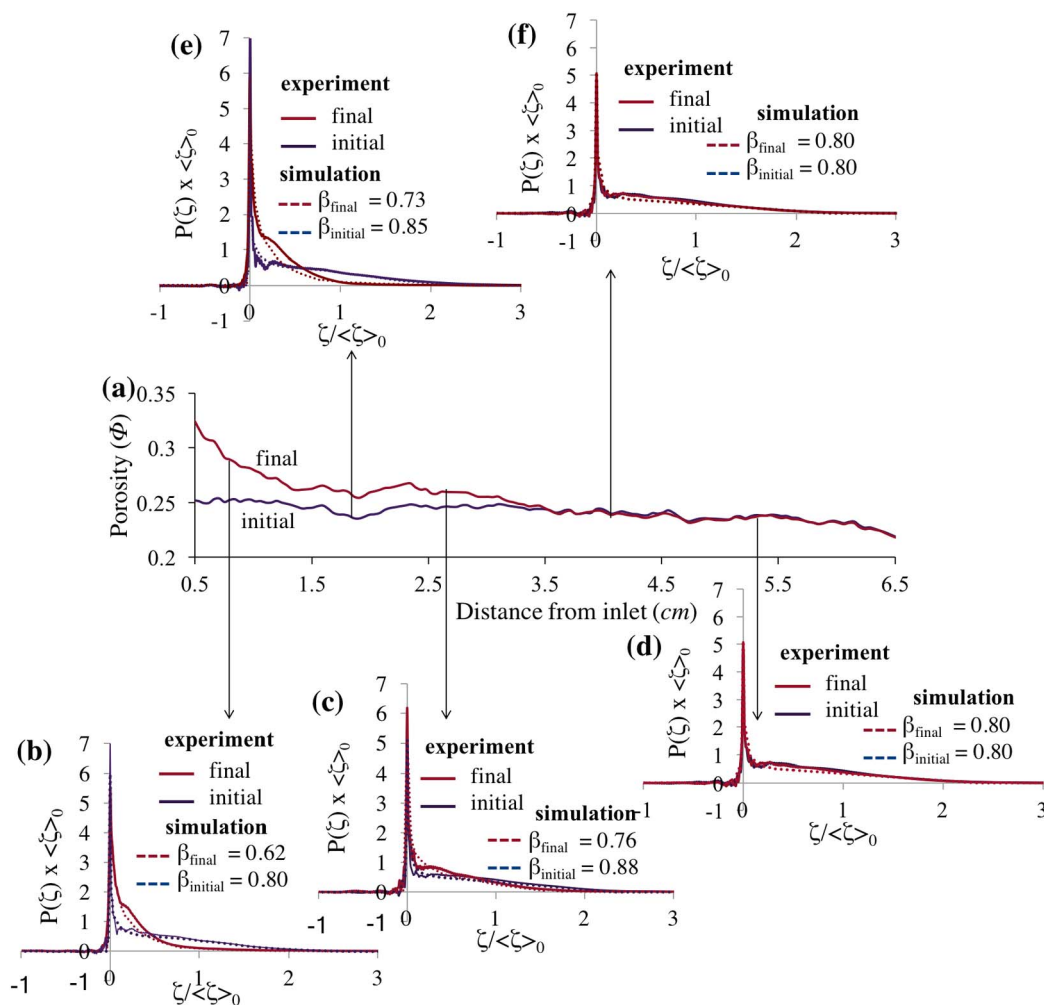


Fig. 7. (a) Evolution of porosities followed by the initial and final (after reaction) propagators at location: (b)  $7.1 \times 10^{-3}$ ; (c)  $2.57 \times 10^{-2}$ ; (d)  $5.22 \times 10^{-2}$ ; (e)  $1.77 \times 10^{-2}$ ; and (f)  $4.16 \times 10^{-2}$  m from the inlet. Propagators are reproduced numerically using  $\psi$  according to Eq. (1). The corresponding  $\beta$ s are shown in the figures. The propagators are matched with experimental data i.e., dotted lines are the computed ones whereas solid lines are measurements.

$v = 3.06 \times 10^{-3} \text{ m s}^{-1}$ . Hence,  $t_1 = l/v$  is 0.0261 s, whereas  $t_2 = l^2/D_m = 3.03 \text{ s}$ . This leaves  $\beta$  as the only tunable parameter. We match our computations in each lattice with the propagators measured within each slice.

In Fig. 7, the porosity profiles at the beginning and the end of the dissolution process are given. Then five propagator profiles at various locations along the core—computed at initial and final times respectively—are plotted and matched with the propagators computed according to unique and different  $\beta$  values. First, it is worthy of note that the numerical results satisfactorily match the experimental data. Second, as dissolution takes place along the core,  $\beta$  values at the front of the experiments become smaller.

As in Section 5.1, the propagators can be computed beyond  $\Delta = 0.25 \text{ s}$ . In Fig. 8, the propagators can be observed, computed initially with  $\beta = 0.8$  and 0.62, with  $t_1$  and  $t_2$  0.0275 and 9.6 s respectively, plotted at observation times  $\Delta$  up to 1.6 s. Our model shows that the stagnant, diffusion dominated regimes persist even at later observation times. Asymptotically, according to Berkowitz et al. (2006), Fickian behaviour should be expected at  $t$  much larger than  $t_2$ .

### 5.3. Core-plug scale CTRW parameters

Transport at the core-plug scale is modelled as a hop governed by  $\psi_{CP}(t)$  which is obtained using the methodology illustrated in Fig. 4. At this scale, transport is modelled in each  $8.8 \times 10^{-4} \text{ m}$ -thick slice of the core using a cubic lattice, with side length  $8.8 \times 10^{-4} \text{ m}$ , consisting of  $100 \times 100 \times 100$  links; see Fig. 9. Particles are injected into the inlet face at  $t = 0$  and record the transit-time required by each particle to reach the outlet face. Transport in each link is governed by  $\psi_P = \psi(\beta_P, t_1, t_2)$  where  $\beta_P$  is calibrated for every slice along the core i.e., by matching the NMR-measured propagators during dissolution. An example of how  $\beta_P$  is obtained has been reported in Section 5.2, i.e. by computing the propagators in each section along the core and matching them with those measured in the experiments.  $t_1 = l/v$  can be determined by knowing the constant flow rate  $Q = 8.3 \times 10^{-7} \text{ m}^3 \text{ s}^{-1}$ , and porosities  $\phi$  of each slice. For example, for the slice where porosity  $\phi = 0.32$ , the interstitial velocity is  $v = 2.74 \times 10^{-3} \text{ m s}^{-1}$ . Hence,  $t_1 = l/v$  is  $3.2 \times 10^{-3} \text{ s}$ . The diffusion cut-off time  $t_2 = l^2/D_m$  is 0.036 s in a single micron-scale link.  $\psi_{CP} = \psi(\beta_{CP})$  for every  $8.8 \times 10^{-4} \text{ m}$ -thick slices are obtained by matching the emergent transit-time distribution with Eq. (1).

$\psi_{CP}(t)$  from  $\psi_P(t)$  are obtained using the upscaling methodology presented in Rhodes et al. (2008), which is illustrated in Fig. 9. First, we run a particle tracking simulation in each core-plug lattice described above. Then, the emergent transit-time distribution  $\psi_{CP}$  is matched with Eq. (1) by selecting the correct  $\beta_{CP}$  value whereas  $t_1$ , and  $t_2$  are assigned according to the lattice dimension, flow rate, and porosities at before and after dissolution. The list of  $\beta_{CP}$  coefficients, and measured porosities, obtained before and after reaction, at a number of points along the core, can be found in Appendix B. After reaction, we found that the

markedly increased porosities especially in the first half of the core near the inlet, do not lead to a more homogeneous spread of particle displacements. Rather, the overall transport process becomes more heterogeneous as shown by the change of propagator profiles before and after reaction. Quantitatively, this is shown by the decrease of  $\beta_{CP}$ . This shows that emergent channels in the core result in some particles experiencing an increase in velocity, whereas other particles who remain in the slower regions now become even more stagnant in comparison. The non-Fickian features are more pronounced after dissolution. This is characterised and quantified by a smaller beta values after dissolution. A smaller beta value means a higher probability of long transit times. This is apparent when seeing the propagator profiles where the most common displacement after dissolution is much smaller than the average.

## 6. Transport at the core scale: obtaining $\psi_C(t)$

At the core scale, transport can be interpreted as a single hop with corresponding  $\psi_C$ . For transport at this scale, a cylindrical lattice is used, see Fig. 10, with length and diameter similar to the core plug used in the experiments. Within each link in the lattice, transport is governed by a transit-time distribution  $\psi_{CP}$ , which has previously been computed. The diameter of the lattice is 3.8 cm, and the length 7.16 cm — identical to the core used in the experiments. The lattice comprises  $40 \times 40 \times 82$  links.

The relation  $\psi_{CP} = Ae^{-t/t_2}(1+t/t_1)^{-1+\beta_{CP}}$  is applied in each link with  $t_1$  and  $t_2$  equal to 0.3 s and 1161 s respectively. 100,000 particles are launched at the inlet face at  $t = 0$  s.

The flux  $Q$  is determined from experiment. Having measured the porosity of every slice along the core, the interstitial velocity  $v$  is computed for every link along the flow direction. The times required for each particle to break through and reach the outlet face are recorded. The emergent transit-time distribution function is plotted for three  $Pe$  numbers—59.3, 593 (the  $Pe$  number of the experiments), and 5930—before and after reaction, see Fig. 11, and have them matched to a functional form i.e., Eq. (1). Thus, the corresponding  $\beta_C$  at initial and final experimental times can be obtained i.e., 0.75 and 0.65 respectively. Note that the power-law behaviour continues to exist at the core, cm, scale.

Prior to reaction, the emergent transit-time distribution function showed a power law behaviour with  $\beta_C = 0.75$ . According to Dentz et al. (2004), in this region i.e.,  $1/2 < \beta < 1$ , the longitudinal dispersion is *super* diffusive. This can be seen from the propagators (Fig. 7). Initially, the bulk of displacement occurs below the mean displacement. With reaction, transport becomes more heterogeneous and even more super-diffusive, as seen in other dissolution experiments (Menke et al., 2016).

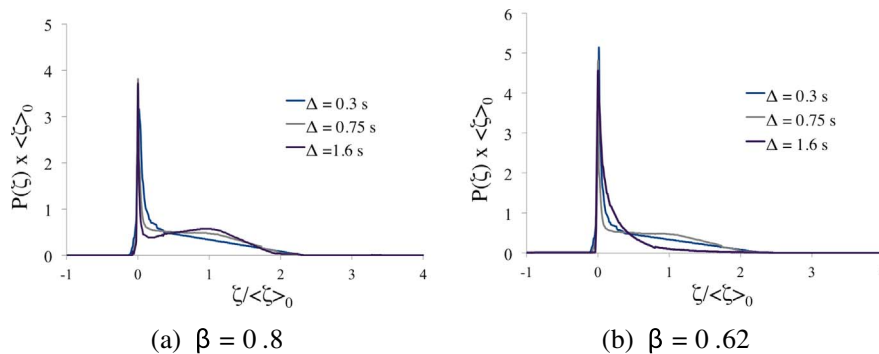


Fig. 8. Prediction of propagators at larger observation times  $\Delta$ . We predict numerically that at around 1.6 s mark, a mobile region at around the main displacement will start to occur.

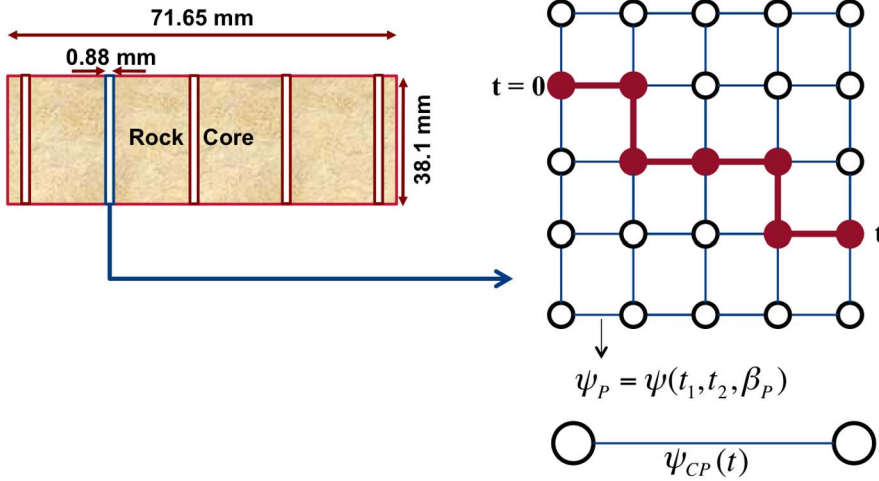


Fig. 9. Transport in each slice along the core is represented as a single hop governed by  $\psi_{CP}(t)$ . Each slice is represented as a 3D lattice consisting of  $100 \times 100 \times 100$  links. In each link, transport is governed by  $\psi_P(t) = \psi(t_1, t_2, \beta_P)$ .  $t_1, t_2$  are computed using the knowledge of flow rate,  $Q = 8.3 \times 10^{-7} \text{ m}^3 \text{ s}^{-1}$ , and porosity  $\phi$ . For each slice,  $\beta_P$  has been calibrated by matching the NMR-measured propagators. Next, we use the upscaling methodology (Rhodes et al., 2008) to obtain  $\psi_{CP}(t)$ .  $\psi_{CP}(t)$  for every slice is tabulated in Appendix B.

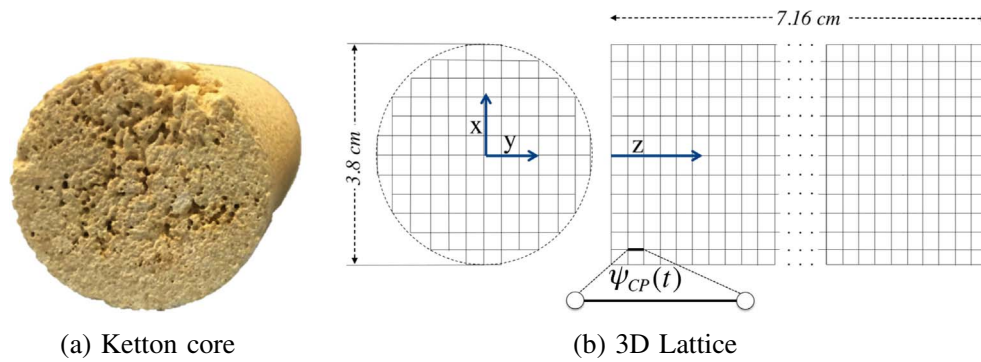
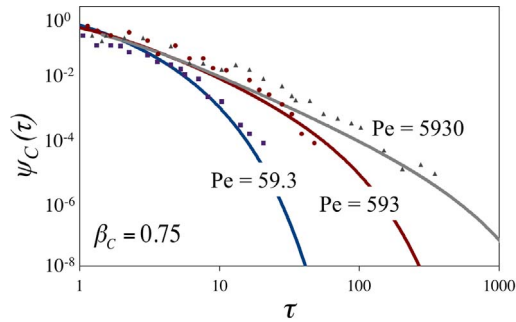
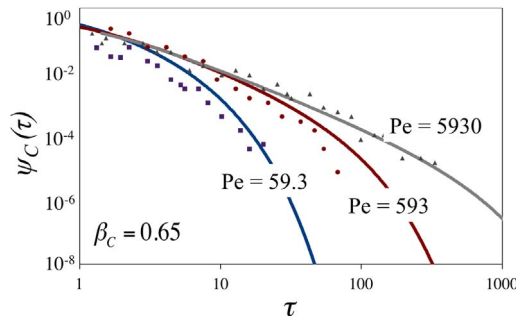


Fig. 10. 3D cylindrical lattice for core-scale simulation with diameter  $3.8 \times 10^{-2} \text{ m}$ , and length  $7.16 \times 10^{-2} \text{ m}$ . The computational domain is a 3D lattice consisting of  $40 \times 40 \times 82$  links.  $v(x, y) = 0$  for  $x^2 + y^2 > (\frac{3.81 \times 10^{-2}}{2})^2 \text{ m}^2$ . Transport in each link is governed by  $\psi_{CP}(t)$ . Then the upscaling method (Rhodes et al., 2008) is used to obtain  $\psi_C(t)$ .



(a) Before reaction



(b) After reaction

Fig. 11. Core-scale ensemble averaged transit-time distribution function  $\psi_C(\tau)$ , at initial  $t_{\text{exp}} = 0$  and final time  $t_{\text{exp}} = 11,800 \text{ s}$ , where  $\tau = t/t_1$  are the normalized transit times. Three  $Pe$  numbers are used where 593 is the  $Pe$  number of the experiments.

## 7. Conclusions

A robust multiscale modelling of transport based on CTRW is validated with a combination of NMR imaging and transport experimentation to study reactive transport signatures at a pore, and core-plug scale. For the specific conditions investigated in our work, the analysis of the propagators before and after reaction show that transport becomes more heterogeneous after reaction. The present model reproduces these results well and quantifies the increase in heterogeneity by the decrease of  $\beta$  values. For a beadpack, Bentheimer sandstone, and Portland carbonate systems, the numerical results agree with the experimental data, validating the pore-scale CTRW model for different porous-media heterogeneities.

By predicting the propagators at longer observation times, it is shown that non-Fickian behaviour persists at the cm scale. Truncated power law behaviour is demonstrated for transport at the core-plug scale, emerging from the pore-scale representation of heterogeneity.

In future work the modelling could be extended to include reactive transport at the pore-scale and hence predict the change in transport properties with time.

## Acknowledgments

The authors would like to thank the Engineering and Physical Science Research Council for financial support through grant numbers EP/L012227/1 and EP/L012251/1. The source codes for the simulations in this paper are available at <https://www.imperial.ac.uk/engineering/departments/earth-science/research/research-groups/perm/research/pore-scale-modelling/software/>.



## Appendix A. Pressure solver

Flow in each link is computed by solving mass conservation equation in each node  $i$  such that for each link  $k$  adjacent to node  $i$ ,  $\sum_k q_k = 0$  applies, or in a matrix form,

$$[B]\mathbf{q} = 0 \quad (\text{A.1})$$

where  $[B]$  is an incidence matrix —  $N_k \times N_i$  where  $N_k$  is the number of links and  $N_i$  is the number of nodes — describing the topology of network.  $\mathbf{q} = q_k$  is the mass flux vector. Applying Darcy's law, flux can be expressed in terms of the pressure drop such that

$$\mathbf{q} = -[C][B]^T \mathbf{p}, \quad (\text{A.2})$$

where  $[C]$  is a conductivity matrix; an  $N_k \times N_i$  diagonal matrix with entries  $C_k = \frac{K_k A_k}{l_k}$  where  $K$  is the permeability of the link,  $A$  the cross-sectional area,  $\mu$  the viscosity and  $l$  the length of the link. Substituting Eq. (A.2) into Eq. (A.1) we derive

$$[B][C][B]^T \mathbf{p} = 0. \quad (\text{A.3})$$

The nodal pressure  $\mathbf{p}$  in the network is obtained by solving the linear Eq. (A.3) using MUMPS: a MULTifrontal Massively Parallel sparse direct Solver — see Amestoy et al. (2001).

## Appendix B. Porosities and the corresponding $\beta_{CP}$ coefficients

The table below shows the porosities and the corresponding  $\beta_{CP}$  coefficients along the core, before and after the experiment. The porosities are measured, whereas the  $\beta_{CP}$  values are computed (see Section 5.3).

Distance from inlet (m $\times 10^{-2}$ )	Porosity $\phi$		$\beta_{CP}$	
	Before	After	Before	After
0.00	0.32	0.59	0.65	0.46
0.09	0.27	0.48	0.77	0.51
0.18	0.26	0.42	0.79	0.51
0.27	0.25	0.38	0.81	0.59
0.35	0.25	0.35	0.80	0.59
0.44	0.25	0.33	0.81	0.61
0.53	0.25	0.32	0.79	0.60
0.62	0.25	0.31	0.83	0.61
0.71	0.25	0.30	0.84	0.62
0.80	0.25	0.29	0.83	0.71
0.88	0.25	0.28	0.82	0.70
0.97	0.25	0.28	0.82	0.71
1.06	0.25	0.28	0.83	0.71
1.15	0.25	0.27	0.82	0.70
1.24	0.25	0.27	0.82	0.75
1.33	0.25	0.26	0.84	0.76
1.42	0.24	0.26	0.84	0.77
1.50	0.25	0.26	0.82	0.76
1.59	0.25	0.27	0.81	0.69
1.68	0.24	0.26	0.86	0.79
1.77	0.24	0.26	0.85	0.73
1.86	0.24	0.26	0.84	0.75
1.95	0.24	0.26	0.84	0.75
2.03	0.24	0.26	0.83	0.74
2.12	0.24	0.26	0.84	0.77
2.21	0.25	0.26	0.85	0.78
2.30	0.25	0.27	0.85	0.78
2.39	0.25	0.26	0.83	0.79
2.48	0.25	0.26	0.87	0.77
2.57	0.24	0.26	0.88	0.80
2.65	0.25	0.26	0.85	0.81
2.74	0.25	0.26	0.85	0.81
2.83	0.25	0.26	0.86	0.79
2.92	0.24	0.26	0.82	0.78
3.01	0.25	0.26	0.84	0.79
3.10	0.25	0.26	0.82	0.80
3.18	0.25	0.25	0.80	0.79
3.27	0.25	0.25	0.79	0.79
3.36	0.24	0.25	0.80	0.78
3.45	0.24	0.25	0.81	0.80
3.54	0.24	0.24	0.80	0.79

3.63	0.24	0.24	0.81	0.81
3.72	0.24	0.24	0.80	0.80
3.80	0.24	0.24	0.81	0.81
3.89	0.24	0.24	0.79	0.79
3.98	0.24	0.24	0.80	0.80
4.07	0.24	0.24	0.81	0.81
4.16	0.24	0.24	0.80	0.80
4.25	0.24	0.24	0.80	0.80
4.33	0.24	0.24	0.80	0.80
4.42	0.24	0.24	0.79	0.79
4.51	0.24	0.24	0.80	0.80
4.60	0.24	0.24	0.83	0.83
4.69	0.23	0.23	0.83	0.83
4.78	0.23	0.23	0.82	0.82
4.87	0.24	0.23	0.85	0.82
4.95	0.24	0.23	0.83	0.82
5.04	0.23	0.23	0.82	0.82
5.13	0.24	0.24	0.80	0.80
5.22	0.24	0.23	0.80	0.80
5.31	0.24	0.24	0.82	0.82
5.40	0.24	0.24	0.80	0.80
5.48	0.24	0.24	0.80	0.80
5.57	0.24	0.24	0.80	0.80
5.66	0.24	0.23	0.80	0.80
5.75	0.23	0.23	0.80	0.80
5.84	0.23	0.23	0.80	0.80
5.93	0.23	0.23	0.81	0.81
6.02	0.23	0.23	0.82	0.82
6.10	0.23	0.23	0.81	0.81
6.19	0.23	0.23	0.83	0.83
6.28	0.23	0.23	0.83	0.83
6.37	0.22	0.22	0.88	0.88
6.46	0.22	0.22	0.87	0.87
6.55	0.22	0.22	0.88	0.88
6.63	0.22	0.22	0.89	0.89
6.72	0.22	0.21	0.88	0.88
6.81	0.22	0.22	0.87	0.87
6.90	0.22	0.22	0.7	0.7
6.99	0.22	0.22	0.71	0.71
7.08	0.22	0.22	0.73	0.73
7.16	0.22	0.22	0.74	0.74

## References

- Amestoy, P.R., Duff, I.S., L'Excellent, J.-Y., Koster, J., 2001. A fully asynchronous multifrontal solver using distributed dynamic scheduling. *SIAM J. Matrix Anal. Appl.* 23 (1), 15–41. <http://dx.doi.org/10.1137/S0895479899358194>. arXiv:<http://dx.doi.org/10.1137/S0895479899358194>.
- Berkowitz, B., Cortis, A., Dentz, M., Scher, H., 2006. Modeling non-Fickian transport in geological formations as a continuous time random walk. *Rev. Geophys.* 44 (2), RG2003. <http://dx.doi.org/10.1029/2005RG000178>.
- Bijeljic, B., Blunt, M.J., 2006. Pore-scale modeling and continuous time random walk analysis of dispersion in porous media. *Water Resour. Res.* 42 (1). <http://dx.doi.org/10.1029/2005wr004578>.
- Bijeljic, B., Mostaghimi, P., Blunt, M.J., 2011. Signature of non-Fickian solute transport in complex heterogeneous porous media. *Phys. Rev. Lett.* 107, 204502. <http://dx.doi.org/10.1103/PhysRevLett.107.204502>.
- Bijeljic, B., Mostaghimi, P., Blunt, M.J., 2013. Insights into non-Fickian solute transport in carbonates. *Water Resour. Res.* 49 (5), 2714–2728. <http://dx.doi.org/10.1002/wrcr.20238>.
- Bijeljic, B., Muggeridge, A.H., Blunt, M.J., 2004. Pore-scale modeling of longitudinal dispersion. *Water Resour. Res.* 40 (11). <http://dx.doi.org/10.1029/2004wr003567>.
- Bijeljic, B., Raeini, A., Mostaghimi, P., Blunt, M.J., 2013. Predictions of non-Fickian solute transport in different classes of porous media using direct simulation on pore-scale images. *Phys. Rev. E* 87, 013011. <http://dx.doi.org/10.1103/PhysRevE.87.013011>.
- Chastanet, J., Wood, B.D., 2008. Mass transfer process in a two-region medium. *Water Resour. Res.* 44 (5). <http://dx.doi.org/10.1029/2006WR005553>. n/a–n/a, W05413.
- Colbourne, A., Sederman, A., Mantle, M., Gladden, L., 2016. Accelerating flow propagator measurements for the investigation of reactive transport in porous media. *J. Magn. Reson.* 272, 68–72. <http://www.sciencedirect.com/science/article/pii/S1090780716301604><http://dx.doi.org/10.1016/j.jmr.2016.08.018>.
- Cortis, A., Gallo, C., Scher, H., Berkowitz, B., 2004. Numerical simulation of non-Fickian transport in geological formations with multiple-scale heterogeneities. *Water Resour. Res.* 40 (4), W04209. <http://dx.doi.org/10.1029/2003WR002750>.
- Degond, P., Lozinski, A., Muljadi, B.P., Narski, J., 2015. Crouzeix-raviart msfem with bubble functions for diffusion and advection-diffusion in perforated media. *Commun. Comput. Phys.* 17 (4), 887–907. <http://dx.doi.org/10.4208/cicp.2014.m299>.
- Dentz, M., Cortis, A., Scher, H., Berkowitz, B., 2004. Time behavior of solute transport in heterogeneous media: transition from anomalous to normal transport. *Adv. Water Resour.* 27 (2), 155–173. <http://www.sciencedirect.com/science/article/pii/S0309170803001726><http://dx.doi.org/10.1016/j.advwatres.2003.11.002>.
- Ederly, Y., Guadagnini, A., Scher, H., Berkowitz, B., 2014. Origins of anomalous transport in heterogeneous media: structural and dynamic controls. *Water Resour. Res.* 50 (2), 1490–1505. <http://dx.doi.org/10.1002/2013WR015111>.
- Freddi, C.N., Hoefner, M.L., Fogler, H.S., 2017. Microemulsion applications in carbonate reservoir stimulation. In: Karunaratne, D.N., Pamunuwa, G., Ranatunga, U. (Eds.), *Properties and Uses of Microemulsions*. InTech, Rijeka. <http://dx.doi.org/10.5772/65973>.
- Herzog, H., Caldeira, K., Reilly, J., 2003. An issue of permanence: assessing the effectiveness of temporary carbon storage. *Clim. Chang.* 59 (3), 293–310. <http://dx.doi.org/10.1023/A:1024801618900>.
- Kang, Q., Chen, L., Valocchi, A.J., Viswanathan, H.S., 2014. Pore-scale study of dissolution-induced changes in permeability and porosity of porous media. *J. Hydrol.* 517, 1049–1055. <http://www.sciencedirect.com/science/article/pii/S0022169414005058><http://dx.doi.org/10.1016/j.jhydrol.2014.06.045>.
- Kärger, J., Heink, W., 1983. The propagator representation of molecular transport in microporous crystallites. *J. Magn. Reson.* (1969) 51 (1), 1–7. <http://www.sciencedirect.com/science/article/pii/002223648390094X>[http://dx.doi.org/10.1016/0022-2364\(83\)90094-X](http://dx.doi.org/10.1016/0022-2364(83)90094-X).

- Li, L., Peters, C.A., Celia, M.A., 2006. Upscaling geochemical reaction rates using pore-scale network modeling. *Adv. Water Resour.* 29 (9), 1351–1370. <http://www.sciencedirect.com/science/article/pii/S0309170805002538><http://dx.doi.org/10.1016/j.advwatres.2005.10.011>.
- Liu, Y., Liu, C., Zhang, C., Yang, X., Zachara, J.M., 2015. Pore and continuum scale study of the effect of subgrid transport heterogeneity on redox reaction rates. *Geochim. Cosmochim. Acta* 163, 140–155. <http://www.sciencedirect.com/science/article/pii/S0016703715002458><http://dx.doi.org/10.1016/j.gca.2015.04.039>.
- Luquot, L., Gouze, P., 2009. Experimental determination of porosity and permeability changes induced by injection of CO<sub>2</sub> into carbonate rocks. *Chem. Geol.* 265 (12), 148–159. <http://www.sciencedirect.com/science/article/pii/S0009254109001600><http://dx.doi.org/10.1016/j.chemgeo.2009.03.028>.
- Menke, H., Andrew, M., Blunt, M., Bijeljic, B., 2016. Reservoir condition imaging of reactive transport in heterogeneous carbonates using fast synchrotron tomography effect of initial pore structure and flow conditions. *Chem. Geol.* 428, 15–26. <http://dx.doi.org/10.1016/j.chemgeo.2016.02.030>.
- Mitchell, J., von der Schulenburg, D.G., Holland, D., Fordham, E., Johns, M., Gladden, L., 2008. Determining NMR flow propagator moments in porous rocks without the influence of relaxation. *J. Magn. Reson.* 193 (2), 218–225. <http://www.sciencedirect.com/science/article/pii/S1090780708001390><http://dx.doi.org/10.1016/j.jmr.2008.05.001>.
- Molins, S., Trebotich, D., Steefel, C.I., Shen, C., 2012. An investigation of the effect of pore scale flow on average geochemical reaction rates using direct numerical simulation. *Water Resour. Res.* 48 (3), W03527. <http://dx.doi.org/10.1029/2011WR011404>.
- Mostaghimi, P., Blunt, M.J., Bijeljic, B., 2013. Computations of absolute permeability on micro-CT images. *Math. Geosci.* 45 (1), 103–125. <http://dx.doi.org/10.1007/s11004-012-9431-4>.
- Muljadi, B.P., 2017. Multiscale method for Oseen problem in porous media with non-periodic grain patterns. *Transp. Porous Media* 116 (1), 1–18. <http://dx.doi.org/10.1007/s11242-016-0762-3>.
- Muljadi, B.P., Narski, J., Lozinski, A., Degond, P., 2015. Nonconforming multiscale finite element method for Stokes flows in heterogeneous media. Part i: methodologies and numerical experiments. *Multiscale Model. Simul.* 13 (4), 1146–1172. <http://dx.doi.org/10.1137/14096428X>. arXiv:<https://doi.org/10.1137/14096428X>.
- Noiriel, C., Gouze, P., Bernard, D., 2004. Investigation of porosity and permeability effects from microstructure changes during limestone dissolution. *Geophys. Res. Lett.* 31 (24), L24603. <http://dx.doi.org/10.1029/2004GL021572>.
- Nunes, J.P., Bijeljic, B., Blunt, M.J., 2015. Time-of-flight distributions and breakthrough curves in heterogeneous porous media using a pore-scale streamline tracing algorithm. *Transp. Porous Media* 109 (2), 317–336. <http://dx.doi.org/10.1007/s11242-015-0520-y>.
- Ovaysi, S., Piri, M., 2014. Pore-space alteration induced by brine acidification in subsurface geologic formations. *Water Resour. Res.* 50 (1), 440–452. <http://dx.doi.org/10.1002/2013WR014289>.
- Peng, C., Crawshaw, J.P., Maitland, G.C., Trusler, J.M., 2015. Kinetics of calcite dissolution in CO<sub>2</sub>-saturated water at temperatures between (323 and 373) K and pressures up to 13.8 MPa. *Chem. Geol.* 403, 74–85. <http://dx.doi.org/10.1016/j.chemgeo.2015.03.012>.
- Porta, G.M., Chaynikov, S., Thovert, J.-F., Riva, M., Guadagnini, A., Adler, P.M., 2013. Numerical investigation of pore and continuum scale formulations of bimolecular reactive transport in porous media. *Adv. Water Resour.* 62, 243–253. <http://www.sciencedirect.com/science/article/pii/S0309170813001590><http://dx.doi.org/10.1016/j.advwatres.2013.09.007>. A tribute to Stephen Whitaker.
- Rhodes, M.E., Bijeljic, B., Blunt, M.J., 2008. Pore-to-field simulation of single-phase transport using continuous time random walks. *Adv. Water Resour.* 31 (12), 1527–1539. <https://dx.doi.org/10.1016/J.Advwatres.2008.04.006>.
- Rhodes, M.E., Bijeljic, B., Blunt, M.J., 2009. A rigorous pore-to-field-scale simulation method for single-phase flow based on continuous-time random walks. *SPE J.* 14, 88–94. <http://dx.doi.org/10.2118/106434-PA>.
- Riva, M., Guadagnini, A., Fernandez-Garcia, D., Sanchez-Vila, X., Ptak, T., 2008. Relative importance of geostatistical and transport models in describing heavily tailed breakthrough curves at the Lauswiesen site. *J. Contam. Hydrol.* 101 (1), 1–13. <http://www.sciencedirect.com/science/article/pii/S016977220800106X><http://dx.doi.org/10.1016/j.jconhyd.2008.07.004>.
- Scheibe, T.D., Murphy, E.M., Chen, X., Rice, A.K., Carroll, K.C., Palmer, B.J., Tartakovsky, A.M., Battiatto, L., Wood, B.D., 2015. An analysis platform for multiscale hydro-geologic modeling with emphasis on hybrid multiscale methods. *Groundwater* 53 (1), 38–56. <http://dx.doi.org/10.1111/gwat.12179>.
- Scheven, U.M., Seland, J.G., Cory, D.G., 2004. NMR propagator measurements on flow through a random pack of porous glass beads and how they are affected by dispersion, relaxation, and internal field inhomogeneities. *Phys. Rev. E* 69, 021201. <http://dx.doi.org/10.1103/PhysRevE.69.021201>.
- Scheven, U.M., Verganelakis, D., Harris, R., Johns, M.L., Gladden, L.F., 2005. Quantitative nuclear magnetic resonance measurements of preasymptotic dispersion in flow through porous media. *Phys. Fluids* 17 (11). <http://scitation.aip.org/content/aip/journal/pof2/17/11/10.1063/1.2131871><http://dx.doi.org/10.1063/1.2131871>. 117107.
- Singurindy, O., Berkowitz, B., Lowell, R.P., 2004. Carbonate dissolution and precipitation in coastal environments: laboratory analysis and theoretical consideration. *Water Resour. Res.* 40 (4). <http://dx.doi.org/10.1029/2003WR002651>. n/a–n/a, W04401.
- Steefel, C.I., DePaolo, D.J., Lichtner, P.C., 2005. Reactive transport modeling: an essential tool and a new research approach for the earth sciences. *Earth Planet. Sci. Lett.* 240 (34), 539–558. <http://www.sciencedirect.com/science/article/pii/S0012821X05005984><http://dx.doi.org/10.1016/j.epsl.2005.09.017>.
- Szymczak, P., Ladd, A.J.C., 2009. Wormhole formation in dissolving fractures. *J. Geophys. Res. Solid Earth* 114 (B6), B06203. <http://dx.doi.org/10.1029/2008JB006122>.
- Tartakovsky, A.M., Meakin, P., Scheibe, T.D., Wood, B.D., 2007. A smoothed particle hydrodynamics model for reactive transport and mineral precipitation in porous and fractured porous media. *Water Resour. Res.* 43 (5), W05437. <http://dx.doi.org/10.1029/2005WR004770>.
- Yang, J., Crawshaw, J., Boek, E.S., 2013. Quantitative determination of molecular propagator distributions for solute transport in homogeneous and heterogeneous porous media using lattice Boltzmann simulations. *Water Resour. Res.* 49 (12), 8531–8538. <http://dx.doi.org/10.1002/2013WR013877>.